Supplementary Information for

Unveil the fundamental understanding of two dimensional π-conjugated FeN_{4+4} sites for boosting peroxymonosulfate activation

Sijia Jin [a], *Wenxian Tan* [a], *Xiaofeng Tang* [a], *Xia Yao* [a], *Yingjian Bao* [a], *Haiyan Zhang* [a,b], *Shuang Song* [a], *Tao Zeng* [*ac]

[a] Key Laboratory of Microbial Technology for Industrial Pollution Control of Zhejiang Province, College of Environment, Zhejiang University of Technology, Hangzhou, Zhejiang 310032, P. R. China

[b] Hangzhou Institute for Advanced Study, University of Chinese Academy of Sciences, Hangzhou, Zhejiang, 310024, P.R. China

[c] Shaoxing Research Institute, Zhejiang University of Technology, Shaoxing, Zhejiang, 312000, PR China

*** Corresponding Author**

Tao Zeng.

Email: zengtao@zjut.edu.cn; Tel: +86-571-88320726.

Text S1. Chemicals and Reagents

Potassium monopersulfate triple salt (PMS, Oxone®, $2KHSO_5 \cdot KHSO_4 \cdot K_2SO_4$), 5,5-dimethyl-1-pyrroline-N-oxide (DMPO), and 2,2,6,6-tetramethylpiperidinyloxyl (TEMP) were purchased from Sigma-Aldrich Chemical Co., Ltd. 1,2,4,5-tetracyanobenzene (BTC), ethylene glycol, N,N-dimethylformamide(DMF), 2,2′-azino-bis(3-ethylbenzothiazoline-6-sulfonic acid) diammonium salt (ABTS) were purchased from Shanghai Macklin Biochemical Co., Ltd. Ferric chloride ($FeCl_3$), cobalt chloride($CoCl_2$), nickel chloride($NiCl_2$), copper chloride($CuCl_2$), 1,2-dicyanobenzene, potassium thiocyanate (KSCN), bisphenol A (BPA), nitroblue tetrazolium chloride (NBT) and sodium azide (NaN_3) were supplied by Aladdin Industrial Corporation. Potassium Iodide (KI), 1,8-diazabicyclo[5.4.0]undec-7-ene (DBU), 1,4-benzoquinone (BQ), L-Histidine (L-His) were obtained from J&K Chemical Co., Ltd. Tert-butanol (TBA), methanol (MeOH), ethanol (EtOH), hydrochloric acid (HCl) and dimethyl sulfoxide (DMSO) were obtained from Sinopharm Chemical Reagent Co., Ltd. All chemicals used in this study were at least in analytical grade without any further purification.

Text S2. Synthesis of CPF-MN_{4+4} (M= Co, Ni, Cu)

Synthesis of CPF-CoN_{4+4}: Similar to the experimental section of CPF-FeN_{4+4}, CPF-CoN_{4+4} was synthesized by treating cobalt chloride (0.130 g, 1 mmol) with 120 mL of mixed solution.

Synthesis of CPF-NiN_{4+4}: Similar to the experimental section of CPF-FeN_{4+4}, CPF-NiN_{4+4} was synthesized by treating nickel chloride (0.129 g, 1 mmol) with 120 mL of mixed solution.

Synthesis of CPF-CuN_{4+4}: Similar to the experimental section of CPF-FeN_{4+4}, CPF-CuN_{4+4} was synthesized by treating copper chloride (0.134 g, 1 mmol) with 120 mL of mixed solution.

Text S3. Characterization

The chemical states of different elements of CPF-MN_{4+4}, CPF, and mono-FeN_{4+4} was detected by X-ray photoelectron spectroscopy (XPS, ESCALAB 250Xi, USA), X-ray diffraction (XRD) patterns were recorded with a PANalytical Empyrean powder diffractometer using Cu Kα radiation (λ= 0.1541 nm). Fourier transform infrared (FTIR) spectroscopy was obtained on Thermo Scientific Nicolet iS20 FTIR spectrometer with KBr as the diluents. X-ray photoelectron spectroscopy (XPS) data were obtained on PerkinElmer PHI 5000 C instrument with a monochromatized Al Kα line source (200 W). The morphology of samples was observed through a field emission scanning electron microscope (FE-SEM, HITACHI Regulus 8100). High-resolution transmission electron microscopy (HRTEM) images were obtained in FEI TalosF200S equipment. The contents of Fe in the samples were quantified by an inductively coupled plasma optical emission spectrometer (ICP-OES, Agilent 720ES). The high-angle annular dark-field scanning transmission electron microscopy (HAADF STEM) images were achieved by FEI Titan Themis 60-300 TEM/STEM. The X-ray absorption find structure spectra (Fe K-edge) were collected at beamline BL44B2 at the SPring-8

synchrotron in Japan. The storage rings of SPring-8 was operated at 8.0 GeV with a maximum current of 250 mA. Using Si (111) double-crystal monochromator, the data collection were carried out in transmission mode using ionization chamber. All spectra were collected in ambient conditions. The electron paramagnetic resonance (EPR) measurements were carried out on a Bruker Model A300 spectrometer.

Text S4. Analytical Methods.

Analysis of BPA concentration was conducted using a Waters e2695 High Performance Liquid Chromatography (HPLC) system, equipped with a UV detector and a C18 column of 4.6 mm × 150 mm and 5 μm particle size. Detection wavelengths were set as 225 nm, 270 nm and 224 nm for BPA, phone and ATZ, respectively, with a mobile phase of methanol/water (70:30, v/v). Further, a mobile phase of methanol/water (60:40, v/v) was set at 280 nm for 4-chlorophenol (4-CP).

The contaminant degradation efficiency (η) is evaluated as Eq. (S1).

$$\eta = \frac{C_0 - C_t}{C_0} \times 100\% \quad \text{(S1)}$$

Where C_0 and C_t are corresponded to the contaminant concentration at initial time and time t (min), respectively.

Total Organic Carbon (TOC) content was determined with a Shimadzu TOC-L Analyzer. Liquid chromatography/mass spectrometry (LC/MS) spectrometry were carried out using an Agilent 1290 (Agilent, USA) liquid chromatograph equipped with a Agilent qtof6550 (Agilent, USA) tandem mass spectrometer. Electrochemical impedance spectroscopy (EIS) and chronoamperometry properties were also evaluated

in a conventional three-electrode cell, with a Pt plate as counter electrode, an Ag/AgCl electrode as reference electrode and an Indium-tin oxide (ITO) glass substrate as working electrode. To prepare the working electrode, a slurry of 20 mg sample dispersed in 300 μL of isopropanol and 50 μL Nafion was sonicated and spread onto pretreated ITO glass. After air-drying, the Scotch tape was unstuck, and the uncoated part was isolated with epoxy resin. PMS concentration was measured using the 2,2'-azino-bis (3-ethylbenzothiazoline-6-sulfonic acid) diammonium salt (ABTS) method. In brief, 0.1 mL of sample was added to a mixture of 0.5 mL of 2 mM ABTS solution, 1 mL of acetate buffer solution (pH = 4), and 20 μL of 1.5 mM potassium iodide (KI) solution, and diluted to 3 mL with water. An absorbance of 415 nm with an absorption coefficient of 34 000 M^{-1} cm^{-1} was detected for each PMS mole, which produced two moles of $ABTS^{\bullet+}$.

Text S5. DFT computational methods

DFT calculations were conducted using the Vienna Ab-inito Simulation Package (VASP), with the exchange-correlation effects described by the Perdew-Burke-Ernzerhof (PBE) functional within the generalized gradient approximation (GGA) method and core-valence interactions accounted for by the projected augmented wave (PAW) method. The energy cutoff for plane wave expansions was set to 450 eV, with structural optimization completed for energy and force convergence set at 1.0×10^{-5} eV and 0.02 eV $Å^{-1}$, respectively. The Brillouin zone was sampled using a 2 × 2 × 1 grid centered at the gamma (Γ) point, while Grimme's DFT-D3 methodology was employed to account for dispersion interactions. The Gibbs free energy changes (ΔG) of the

reaction were then calculated as $\Delta G = \Delta E + \Delta ZPE - T\Delta S$, wherein ΔE is the electronic energy difference directly obtained from DFT calculations, ΔZPE is the zero-point energy difference, T is the room temperature (298.15 K) and ΔS is the entropy change.[1, 2]

Text S6. The calculation of normalized k_{obs} (K_N)

The calculation of K_N (normalized k_{obs}, min^{-1} L^2 g^{-2}):

$$K_N = \frac{k_{obs}}{[PMS] \times [Cat.]}$$

where k_{obs} is the observed reaction rate constant (min^{-1}), [PMS] and [Cat.] are the dose of the catalyst (g L^{-1}) and PMS (g L^{-1}), respectively

Table S1. EXAFS fitting parameters at the Fe K-edge for various samples

Sample	Shell	*CN*[a]	*R*(Å)[b]	σ2 (Å^2·10^{-3}) [c]	ΔE_0(eV)[d]	R factor (%)
Fe Foil	Fe-Fe_1	8*	2.46±0.006	0.0049	4.51±1.12	0.6
	Fe-Fe_2	6*	2.83±0.014	0.0061	6.90±2.12	
Fe_2O_3	Fe-O_1*	3*	1.93±0.007	0.0069	3.52±0.23	1.1
	Fe-O_2*	3*	2.07±0.020	0.0040	5.17±1.15	
Fe Pc	Fe-N	4*	1.93±0.021	0.0047	3.64±1.22	0.7
FeO	Fe-O*	6*	2.14±0.023	0.0050	0.85±3.20	0.7
CPF-FeN_{4+4}	Fe-N	3.9±0.2	1.92±0.011	0.0058	6.71±2.07	0.6

[a]*CN*, coordination number; [b]*R*, distance between absorber and backscatter atoms; [c]σ^2, Debye-Waller factor to account for both thermal and structural disorders; [d]ΔE_0, inner potential correction; *R* factor indicates the goodness of the fit. $S0^2$ was fixed to 0.78, according to the experimental EXAFS fit of Fe foil by fixing CN as the known crystallographic value. Fitting range: $3.0 \le k$ (/Å) ≤ 12 and $1.5 \le R$ (Å) $\le$ ~3.2 (Fe foil); $3.0 \le k$ (/Å) ≤ 12.0 and $1.0 \le R$ (Å) $\le$ ~2.2 (Sample Fe). A reasonable range of EXAFS fitting parameters: $0.700 < S_0^2 < 1.000$; $CN > 0$; $\sigma^2 > 0$ Å^2; $\Delta E_0 < 10$ eV; *R* factor < 0.02.

Table S2. Kinetics comparison of micropollutants degradation of by CPF-FeN_{4+4}/PMS and other single-atom catalyst/PMS systems.

Catalysts	PMS dosage (g/L)	Catalyst dosage (g/L)	Contaminant (μM)	k_{obs}	K_N	Ref.
Co-C-600	0.25	0.1	SMX (40 μM)	0.071	2.84	[3]
FeSA-N-CNT	0.25	0.02	BPA (50 μM)	0.102	20.40	[4]
Co–N–CNTs	0.6	0.1	SMX (40 μM)	0.175	1.05	[5]
NiSACs@CN	0.4	0.05	SMX (40 μM)	0.129	6.45	[6]
Co-SA	0.3	0.2	CIP (60 μM)	0.140	2.33	[7]
1.2Fe–N–C	0.2	0.15	Phenol (200 μM)	0.328	10.93	[8]
SA Cu/Graphene	0.8	0.1	SMX (40 μM)	0.088	1.10	[9]
Fe_{SA}-BC	0.6	0.2	BPA (40 μM)	0.158	1.32	[10]
SA Fe-OCN	0.6	0.5	Phenol (100 μM)	0.039	0.13	[11]
Cu-N_4/C-B	0.2	0.1	BPA (88 μM)	0.56	28.00	[12]
Co-CN	0.031	0.03	Phenol (200μM)	0.014	15.05	[13]
CoSAC-NG	0.6	0.005	BPA (20 μM)	0.044	14.66	[14]
Co-N_3O_1	0.307	0.1	CIP (15μM)	0.287	9.35	[15]
CPF-FeN_{4+4}	0.1	0.1	BPA (20 μM)	1.87	187.00	This work

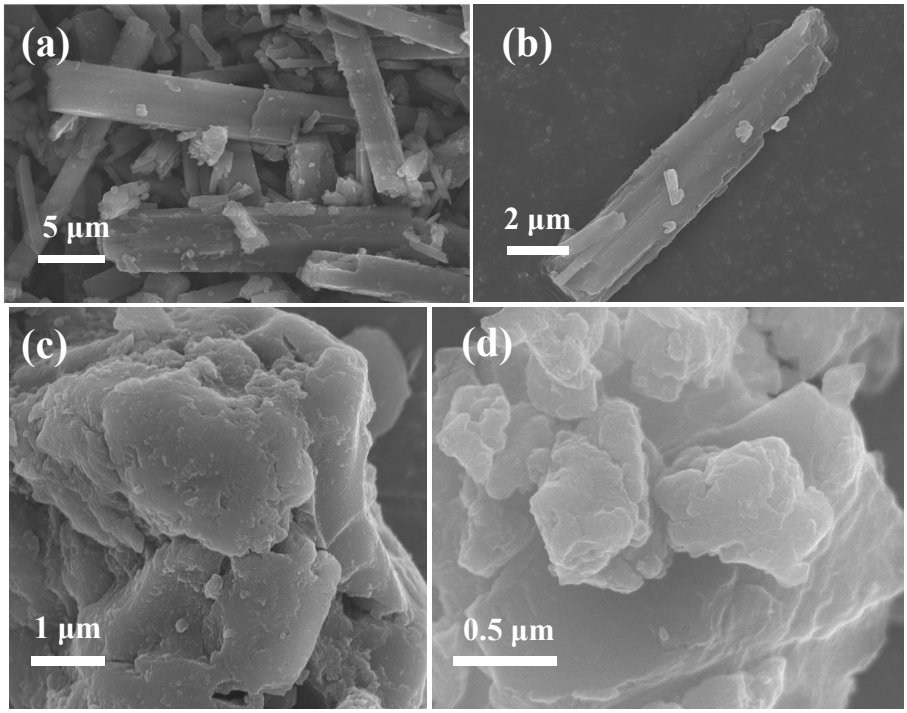

123

124 **Figure S1.** FE-SEM image of (a-b) mono-FeN_{4+4} and (c-d) CPF-FeN_{4+4}

125

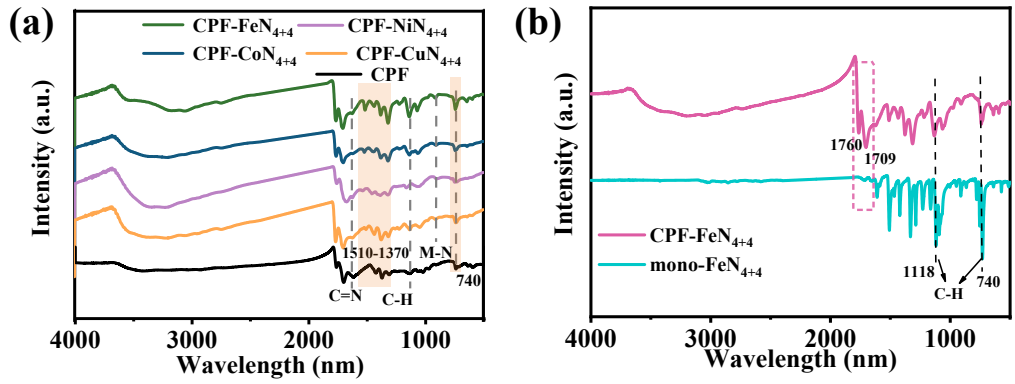

126

127 **Figure S2.** FTIR spectra of (a) CPF, CPF-MN_{4+4} (M=Fe, Co, Ni, Cu), (b) CPF-FeN_{4+4},

128 and mono-FeN_{4+4}.

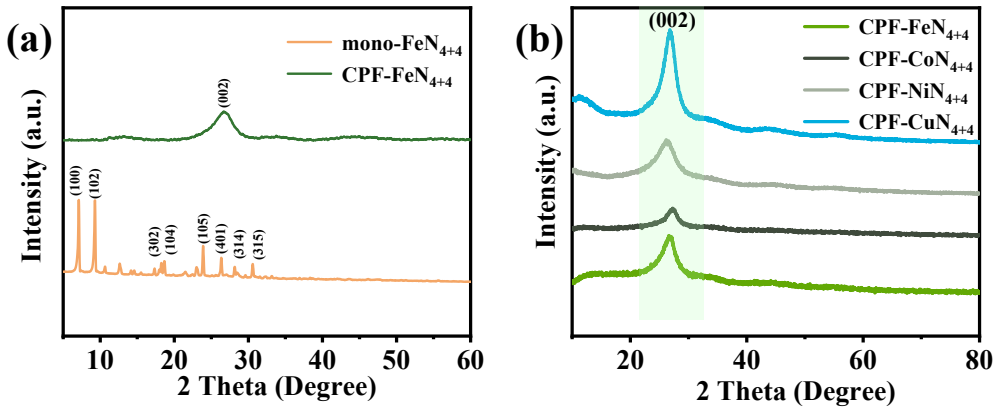

129

130 **Figure S3.** (a) XRD spectra of CPF- FeN_{4+4}, mono-FeN_{4+4} and (b) CPF-MN_{4+4} (M=Fe,

131 Co, Ni, Cu).

132

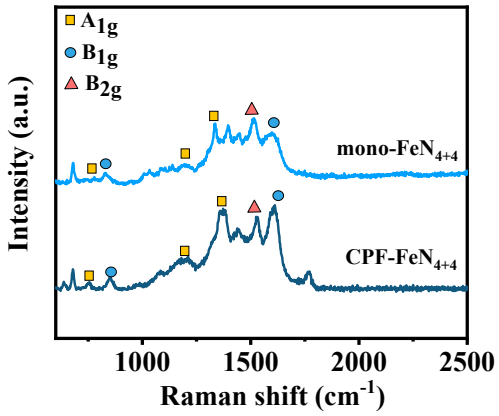

133

134 **Figure S4** Raman spectra of CPF-FeN_{4+4}, and mono-FeN_{4+4}.

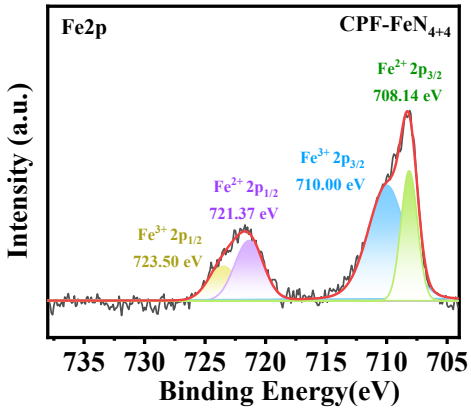

135

136 **Figure S5.** XPS Fe 2p spectra of CPF-FeN_{4+4}.

137

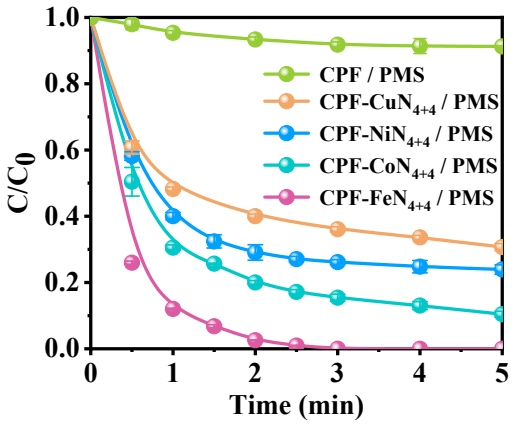

138

139 **Figure S6.** The different metal catalyst systems of BPA degradation.

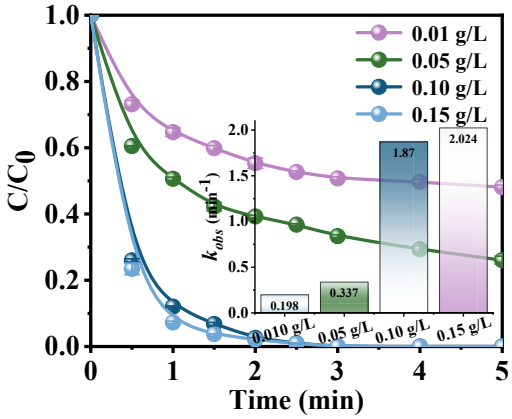

140

141 **Figure S7** The effect of catalyst dosage on the removal of BPA in CPF-FeN_{4+4}/PMS

142 system. Routine conditions: [BPA] = 20 μM, [PMS] = 0.15 mM, temperature = 25 °C,

143 without pH adjustment.

144

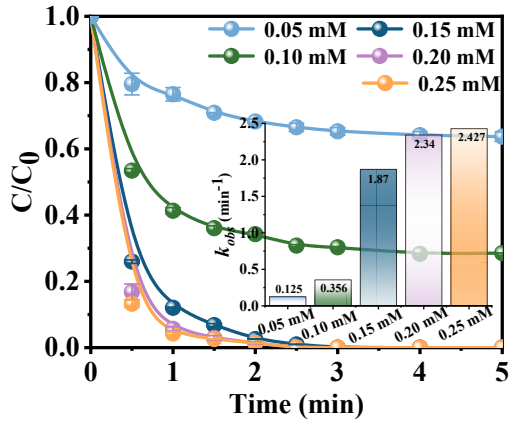

145

146 **Figure S8.** The effect of PMS dosage on the removal of BPA in CPF-FeN_{4+4}/PMS

147 system. Routine conditions: [BPA] = 20 μM, [catalyst] = 0.10 g/L, temperature = 25

148 °C, without pH adjustment.

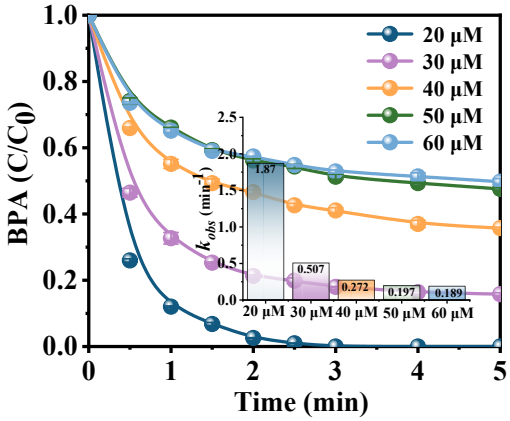

149

150 **Figure S9.** The effect of BPA concentration on the removal of BPA in CPF-
151 FeN_{4+4}/PMS system. Routine conditions: [catalyst] = 0.10 g/L, [PMS] = 0.15 mM,
152 temperature = 25 °C, without pH adjustment.

153

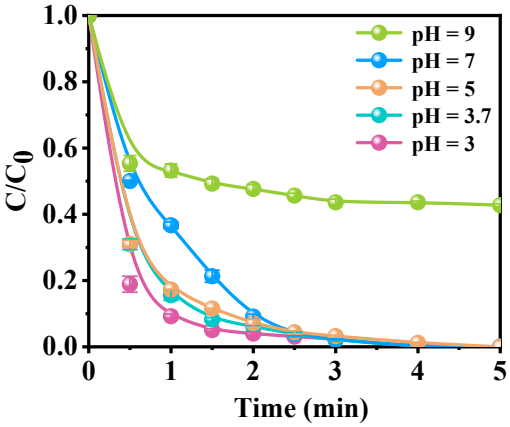

154

155 **Figure S10.** The effect of pH on the removal of BPA in CPF-FeN_{4+4}/PMS system.
156 Routine conditions: [BPA] = 20 μM, [catalyst] = 0.10 g/L, [PMS] = 0.15 mM,
157 temperature = 25 °C.

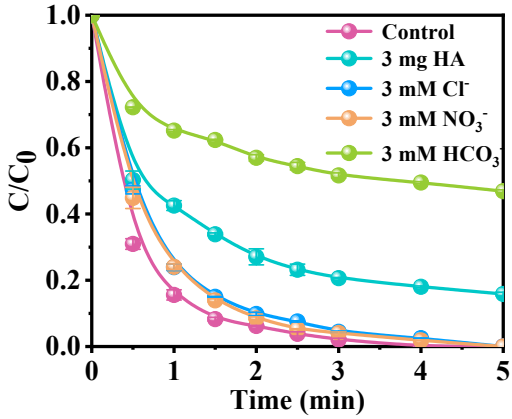

158

159 **Figure S11.** The effects of inorganic anions (HCO_3^-, NO_3^- and Cl^-) and HA on the
160 removal of BPA in CPF-FeN_{4+4}/PMS system. Routine conditions: [BPA] = 20 μM,
161 [catalyst] = 0.10 g/L, [PMS] = 0.15 mM, temperature = 25 °C, without pH adjustment.

162

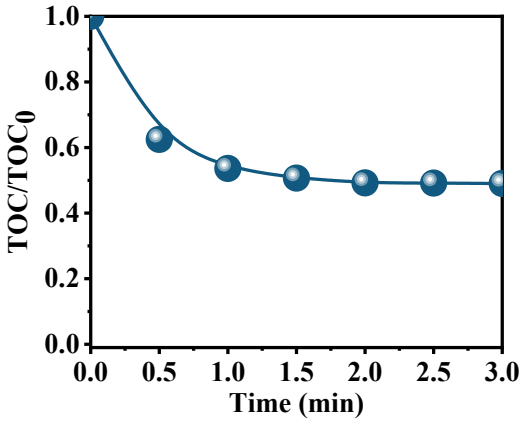

163

164 **Figure S12.** TOC removal of BPA in CPF-FeN_{4+4}/PMS system.

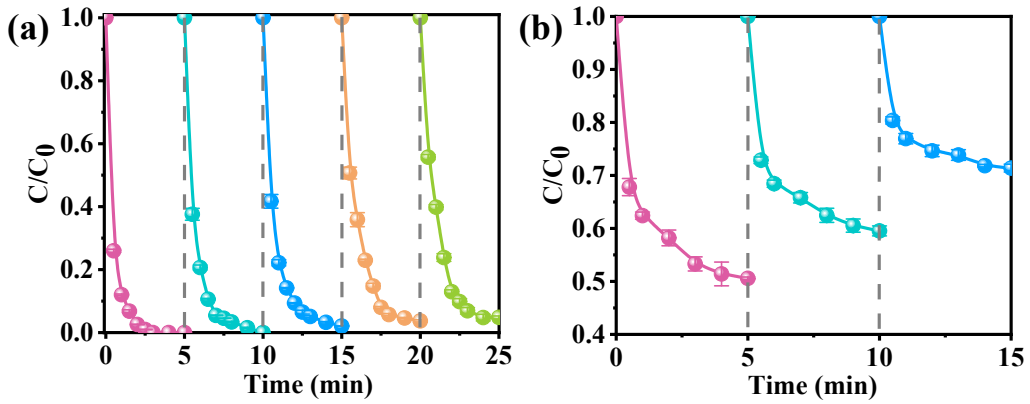

165

166 **Figure S13.** Recyclability of (a) CPF-FeN_{4+4}/PMS system and (b) mono-FeN_{4+4}/PMS

167 system for BPA removal. Routine conditions: [BPA] = 20 μM, [catalyst] = 0.10 g/L,

168 [PMS] = 0.15 mM, temperature = 25 °C, without pH adjustment.

169

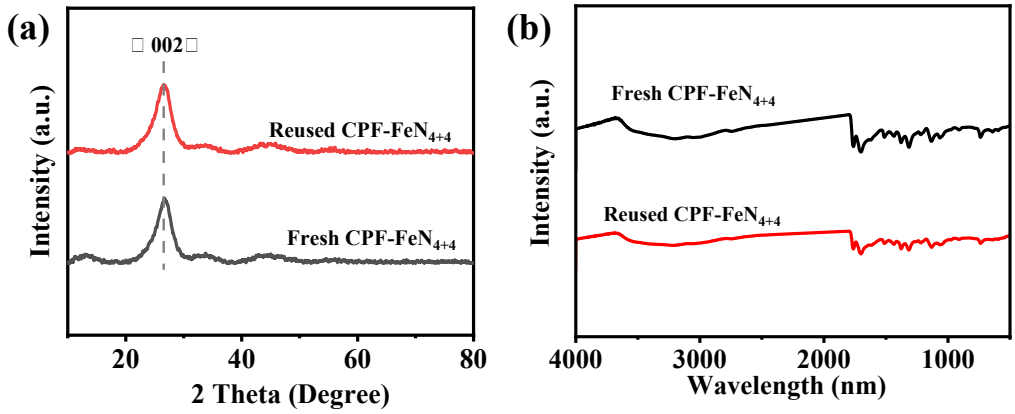

170

171 **Figure S14.** (a) XRD patterns of fresh and reused CPF-FeN_{4+4}. (b) FTIR spectra of

172 fresh and reused CPF-FeN_{4+4}.

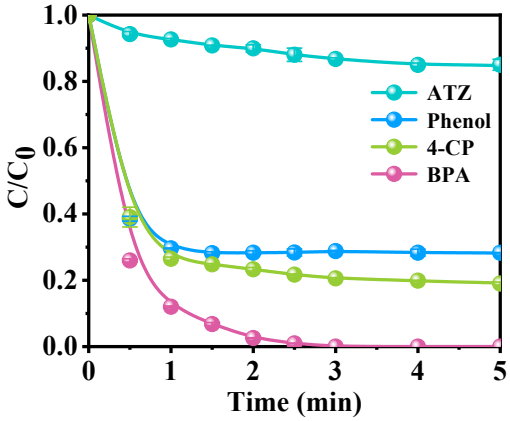

173

174 **Figure S15.** Different pollutants removal in CPF-FeN_{4+4}/PMS system.

175

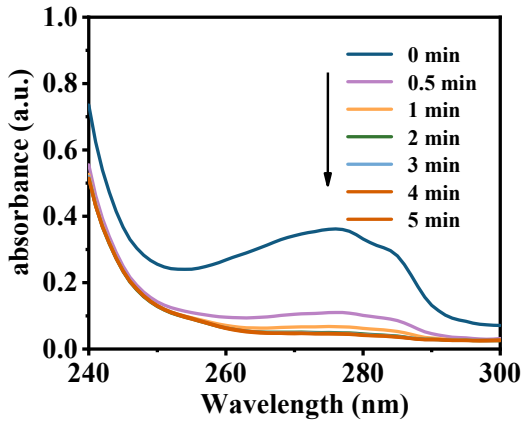

176

177 **Figure S16.** Spectra of NBT transformation generated by CPF-FeN_{4+4}/PMS system.

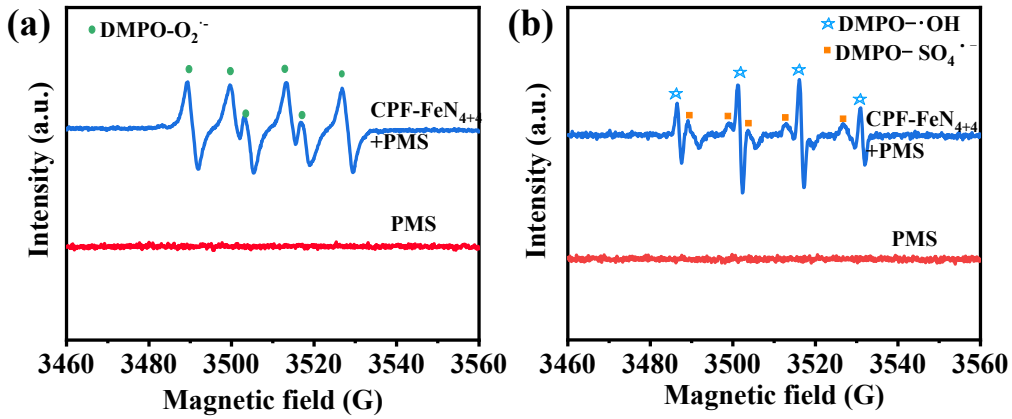

178

179 **Figure S17.** (a) EPR spectra of different systems using DMPO in MeOH as the spin-
180 trapping agent. (b) EPR spectra of different systems using DMPO in H_2O as the spin-
181 trapping agent.

182

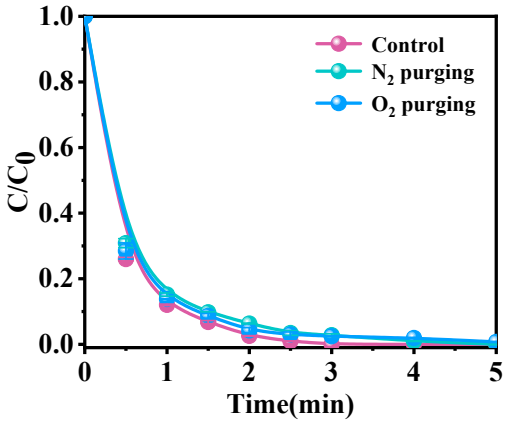

183

184 **Figure S18.** Effect of N_2 and O_2 purging in CPF-FeN_{4+4}/PMS system on BPA removal.

185

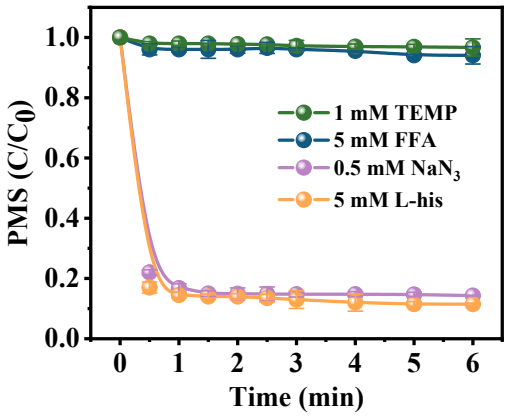

186

187 **Figure S19.** Decomposition rate of PMS with different quenchers. Routine conditions:

188 [PMS] = 0.15 mM, temperature = 25 °C, without pH adjustment.

189

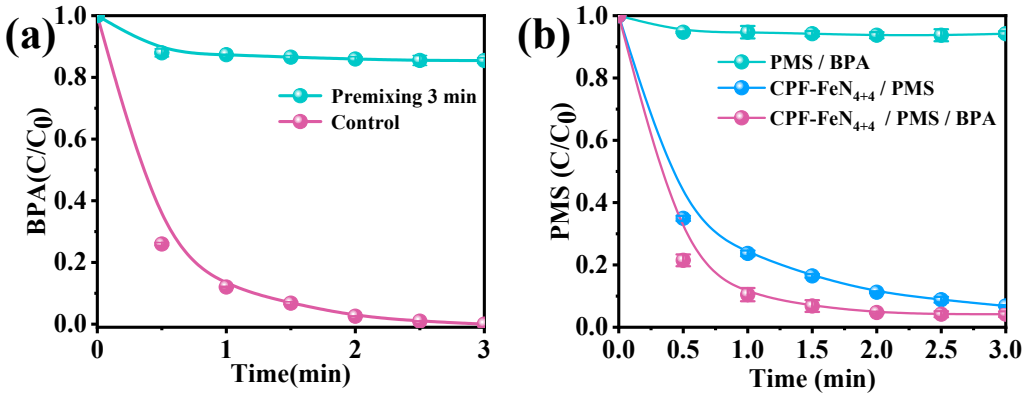

190

191 **Figure S20.** (a) Effect of permixing in CPF-FeN_{4+4}/PMS system on BPA removal. (b)

192 Decomposition rate of PMS in different systems. Routine conditions: [BPA] = 20 μM,

193 [catalyst] = 0.10 g/L, [PMS] = 0.15 mM, temperature = 25 °C, without pH adjustment.

194

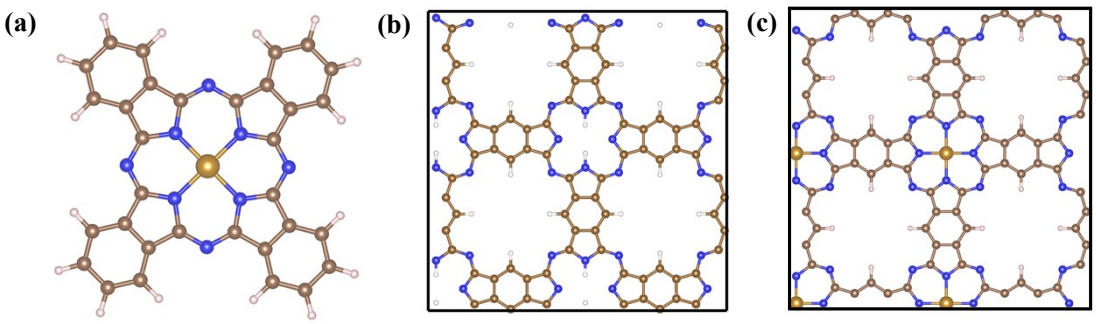

Figure S21. Top view structures of (a) mono-FeN_{4+4}, (b) CPF and (c) CPF-FeN_{4+4} models.

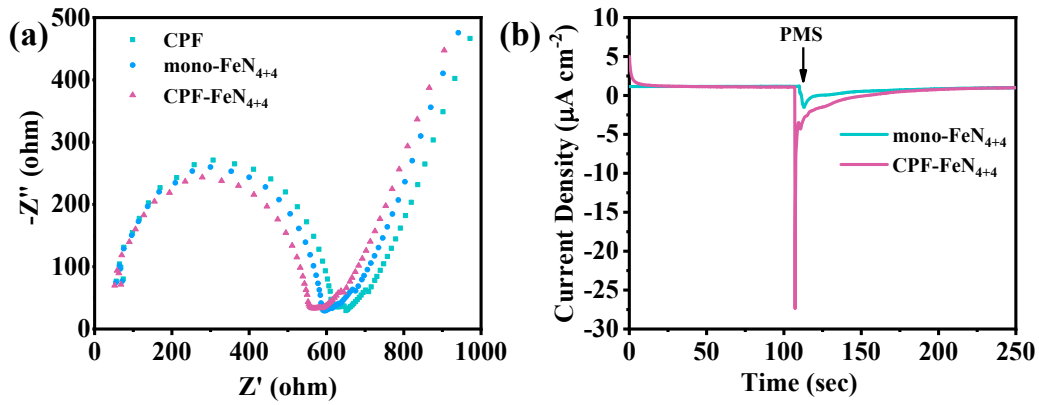

Figure S22. (a) electrochemical impedance analyses spectra of CPF-FeN_{4+4}, mono-FeN_{4+4} and CPF. (b)The I-t curves of CPF-FeN_{4+4} and mono-FeN_{4+4}.

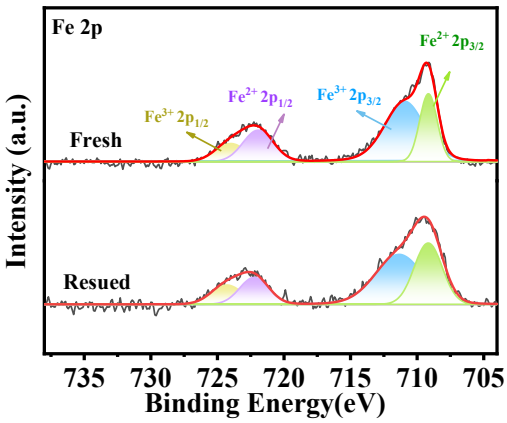

202

203 **Figure S23.** XPS Fe 2p spectra of fresh and reused CPF-FeN_{4+4}.

204

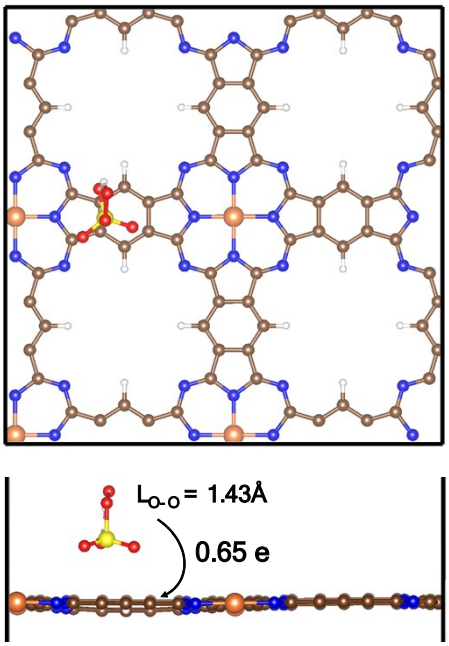

205

206 **Figure S24.** Top and side view of CPF-FeN_{4+4} adsorbing PMS on C site.

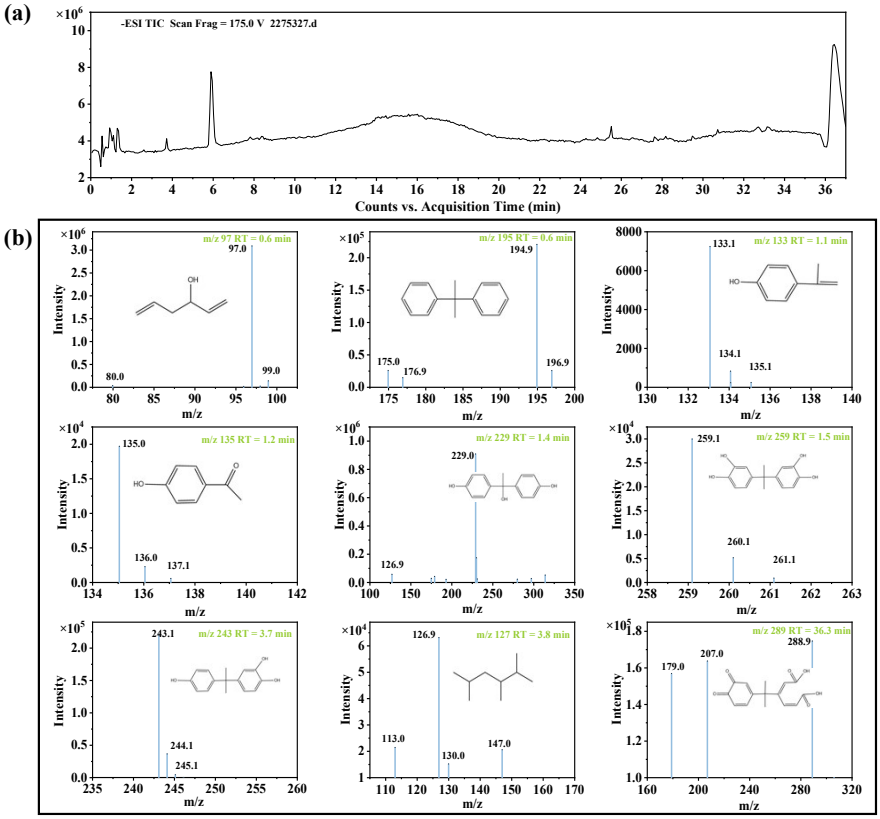

Figure S25. LC/MS chromatogram and mass spectra for BPA. (a) total ions chromatogram (TIC) from LC-MS; (b) mass spectra of the main peaks. Routine conditions: [BPA] = 20 μM, [catalyst] = 0.10 g/L, [PMS] = 0.15 mM, temperature = 25 °C, without pH adjustment.

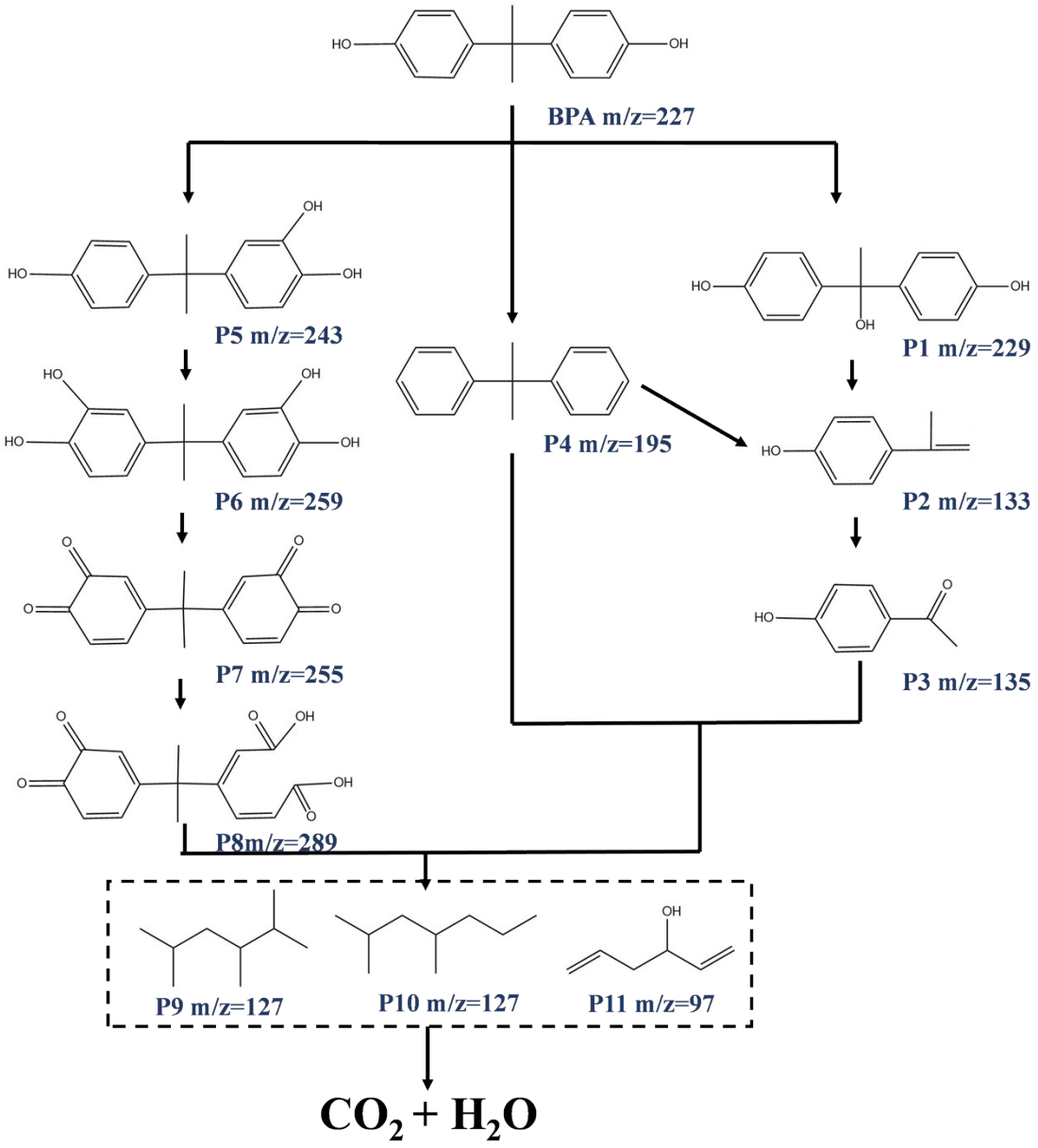

212

213 **Figure S26.** Proposed degradation pathway of BPA over CPF-FeN_{4+4}/PMS system.

References

1. J. P. Perdew, K. Burke and M. Ernzerhof, *Phys. Rev. Lett.* 1996, **77**, 3865-3868.
2. J. Hafner, *J. Comput. Chem.* 2008, **29**, 2044-2078.
3. S. Wang and J. Wang, *Appl. Catal. B* 2023, **321**, 122051.
4. K. Qian, H. Chen, W. Li, Z. Ao, Y. N. Wu and X. Guan, *Environ. Sci. Technol.* 2021, **55**, 7034-7043.
5. J. Miao, Y. Zhu, J. Lang, J. Zhang, S. Cheng, B. Zhou, L. Zhang, P. J. J. Alvarez and M. Long, *ACS Catal.* 2021, **11**, 9569-9577.
6. J. Yang, P. Li, X. Duan, D. Zeng, Z. Ma, S. An, L. Dong, W. Cen and Y. He, *J. Hazard. Mater.* 2022, **430**, 128463.
7. X. Mi, P. Wang, S. Xu, L. Su, H. Zhong, H. Wang, Y. Li and S. Zhan, *Angew. Chem. Int. Ed.* 2021, **60**, 4588-4593.
8. J. He, Y. Wan and W. Zhou, *J. Hazard. Mater.* 2021, **405**, 124199.
9. F. Chen, X.-L. Wu, L. Yang, C. Chen, H. Lin and J. Chen, *Chem. Eng. J.* 2020, **394**, 124904.
10. F. Li, Z. Wan, D. Zheng, L. Zhang, W. Huang, F. Chen, J. Deng, Z. Qi, G. Li and F. Zhang, *Chem. Eng. J.* 2024, **482**, 149052.
11. Z. Zhou, M. Li, C. Kuai, Y. Zhang, V. F. Smith, F. Lin, A. Aiello, D. P. Durkin, H. Chen and D. Shuai, *J. Hazard. Mater.* 2021, **418**, 126294.
12. X. Zhou, M. K. Ke, G. X. Huang, C. Chen, W. Chen, K. Liang, Y. Qu, J. Yang, Y. Wang, F. Li, H. Q. Yu and Y. Wu, *Proc. Nat. Acad. Sci.* 2022, **119**, e2119492119.
13. Q. Y. Wu, Z. W. Yang, Z. W. Wang and W. L. Wang, *Proc. Nat. Acad. Sci.* 2023, **120**, e2219923120.
14. H. Q. Zhao, J. S. Song, P. Lu and Y. Mu, *Chem. Eng. J.* 2023, **456**, 141045.
15. Z. Wang, E. Almatrafi, H. Wang, H. Qin, W. Wang, L. Du, S. Chen, G. Zeng and P. Xu, *Angew. Chem. Int. Ed.* 2022, **61**, e202202338.